Temperature Estimation Using Lumped-Parameter Thermal Network With Piecewise Stator-Housing Modules for Fault-Tolerant Brake Systems in Highly Automated Driving Vehicles

Baik-Kee Song, Jun-Woo Chin, Dong-Min Kim, Kyu-Yun Hwang, and Myung-Seop Lim, *Member, IEEE*

***Abstract*— With the increased interest in intelligent transportation, the need for fault-tolerant systems has also increased. In this paper, we propose a piecewise stator-housing module (PSM) and construct a lumped-parameter thermal network (LPTN) that can be used in a fault-tolerant system based on the PSM. The proposed LPTN model considers not only radial and axial heat transfer but also tangential heat transfer; therefore, even if only one of the two circuits is running on a fault-tolerant motor (dual winding motor), the coil temperature can be estimated. To verify the proposed model, three winding-type motors are tested with varying current values during normal and fault operations, and the test and analysis results are in good agreement. Additionally, the usefulness of the proposed model is demonstrated by comparing the temperatures of both the conventional and proposed LPTNs in the event of a brake system fault during braking operation in a virtual traffic jam simulation. This simulation demonstrates that temperature estimation of the motor is important for motor design because the brake operation time is dependent on the motor temperature. Furthermore, the system performance or size can be determined by accurately predicting the temperature, even in the event of a fault in the brake system, where the fault-tolerant motor is used, thus keeping the driver safe. The proposed LPTN can be used in brake systems and in other systems that utilize fault-tolerant dual winding motors.**

***Index Terms*— Brake systems, dual winding motor, fault-tolerant motor, highly automated driving (HAD), integrated electronic brake (IEB), lumped parameter thermal network (LPTN), piecewise stator-housing module (PSM), temperature, thermal analysis, thermal resistance.**

I. Introduction

RECENTLY, with the expansion of R&D in electric vehicles (EVs), hybrid electric vehicles (HEVs) and plug-in HEVs (PHEVs) due to emission regulations, hydraulic and mechanical vehicular systems are being converted into electronic systems to improve energy efficiency. The motor plays an important role in this stage of development. Automotive companies are attempting to improve the fuel efficiency of conventional engines to meet the Euro 6 standard, while efforts are being made to reduce the weight of each part in an EV to increase the mileage under a full charge. Similarly, the sizes of motors, which are the main power sources of eco-friendly vehicles, are also being reduced. It is necessary to consider the coil temperature of the motor to satisfy the operation time for the required load while minimizing the motor size. In addition, the development of electric power based vehicle systems has resulted in the era of autonomous driving, and fault-tolerant systems are required to ensure driver safety. There is an increased demand for fault-tolerant motors for highly automated driving (HAD) vehicles, which is being studied in terms of motor hardware and control.

Zhao *et al.* [1], El-Refaie [2] studied the advancement of the technologies of permanent magnet (PM)-based fault-tolerant machines. Zhao *et al.* [3] investigated the fault-tolerant performance of a doubly salient brushless DC generator. Mao *et al.* [4], [5] proposed the use of adaptive control to compensate for actuator failure by considering train motion dynamics. Moradi and Fekih [6] designed a fault-tolerant PID control scheme with a vehicle suspension system for actuator faults. Wang *et al.* [7] proposed distributed fault-tolerant control for a group of nonlinear systems consisting of multiple interconnected subsystems. Yang *et al.* [8] studied the implementation of hybrid fault-tolerant control for four-wheel steering and four-wheel drive EVs to maintain the tracking performance of the vehicles by considering the faults, input constraints, and external resistance. Zhang *et al.* [9] proposed a fault-tolerant direct torque control algorithm for a five-phase PM motor based on three-phase space vector pulse-width modulation. In addition, regarding electrical brake control, studies have been conducted on optimized cooperative control between the brake motor and the traction motor [10]–[12] and brake control using an in-wheel motor according to road conditions in pure EVs [13], [14].

In addition, the sensorless control of motors has been investigated. Rotor position information is required for motor

Manuscript received June 30, 2020; revised December 20, 2020 and May 7, 2021; accepted June 15, 2021. Date of publication July 9, 2021; date of current version September 1, 2021. This work was supported by the National Research Foundation of Korea (NRF) grant funded by the Korea government (MSIT) under Grant NRF-2020R1A4A4079701. The Associate Editor for this article was T. Q. Dinh. *(Corresponding author: Myung-Seop Lim.)*

Baik-Kee Song, Jun-Woo Chin, and Myung-Seop Lim are with the Department of Automotive Engineering, Hanyang University, Seoul 04763, South Korea (e-mail: songbk82@gmail.com; cjw1254@hanyang.ac.kr; myungseop@hanyang.ac.kr).

Dong-Min Kim is with the Department of Automotive Engineering, Honam University, Gwangju 62399, South Korea (e-mail: kimdmin@honam.ac.kr).

Kyu-Yun Hwang is with the Global Research and Development Center, Mando, Seongnam 13486, South Korea (e-mail: kyuyun7@hanmail.net).

Digital Object Identifier 10.1109/TITS.2021.3091621

1558-0016 © 2021 IEEE. Personal use is permitted, but republication/redistribution requires IEEE permission.
See https://www.ieee.org/publications/rights/index.html for more information.

Authorized licensed use limited to: Hanyang University. Downloaded on June 22,2022 at 01:52:54 UTC from IEEE Xplore. Restrictions apply.

control, thus, a position sensor such as a resolver or an encoder is needed. However, these electronic devices reduce the reliability of HAD systems. Therefore, sensorless control that can retain the rotor position information even when the position sensor is eliminated has been studied. There are several methods of sensorless control, each of which has strengths and weaknesses [15]. In particular, the rotor position cannot be accurately determined for the control method that uses flux linkage. This is because the flux linkage is significantly low or zero when the speed is low or stationary. Therefore, studies have been conducted to solve this problem [16]–[18]. Research has also been conducted to reduce the error between the estimated position and the actual position of the rotor due to the difference in inductance by selecting the PWM injection frequency [19]–[21]. A sensorless method using a sliding mode observer (SMO) has also been developed, and studies on methods that are robust to parameter changes and time delay have been conducted [22]–[24]. A control method in the form of a combination of SMO and modified fundamental excitation PWM (FPE) [23], or a combination of SMO and phase-locked loop filters [24], has been studied. Most of the studies mentioned above focus on the topologies, performance, and control method of the motor considering fault tolerance. However, there are few conducted on the method of predicting the temperature of the internal coil of the motor, which is an important design factor, when the fault tolerant system encounters a fault.

In this study, automotive braking systems were developed that use dual winding motors in which the circuit is divided into two, for use in fault-tolerant systems. During normal operations, the motor current flows to both circuits to generate torque. If any one of the circuits is not available due to a specific problem, current flows to an available circuit to generate torque to enable the system's minimum performance. However, while maintaining this minimum performance, the coil may be damaged owing to current overflow to the circuit, in contrast to the case during normal operation. Therefore, when designing a motor, the coil temperature should be considered for the operating current in the event of a fault. When designing a motor, various methods such as computational fluid dynamics (CFD), finite-element analysis (FEA), and lumped parameter thermal networks (LPTNs) are used to predict the temperature of the motor coil. CFD reflects convective heat transfer inside and outside the motor well. An advantage of FEA is that it can analyze heat transfer by conduction well; however, it involves long modeling and analysis times. To avoid errors in numerical analyses, accurate modeling and boundary conditions are applied. Therefore, LPTNs, which include reasonable errors, but are quick and easy to analyze, have attracted the attention of motor designers [25], [26]. An LPTN can consider convection, conduction, and radiation heat transfers, and its analysis time is short. However, the accuracy of the analysis can be improved by setting empirical values such as the coil conductivity including coating and fill factor and convective heat-transfer coefficient.

Therefore, studies have been conducted to determine the thermal conductivity of the coils by considering the fill factor and the coefficients of convective and radiative heat transfer [27]–[41]. However, the existing lumped circuits focus mainly on predicting the temperature in the case of normal driving; this implies that the current flows through all coils of the stator.

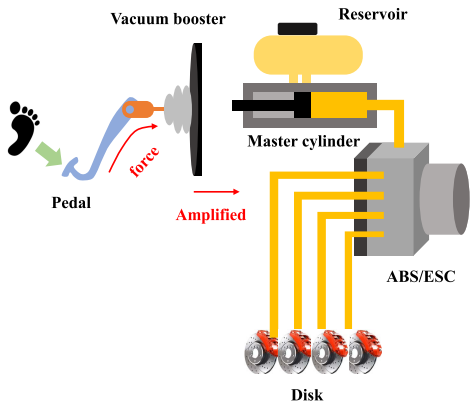

Fig. 1. Conventional brake system having an antilock brake system(ABS) with electronic stability control (ESC).

Based on previous studies, this paper proposes an LPTN that can predict the temperature of a fault mode in which the current flows only in a part of the entire coil of the stator in a dual winding motor. The authors propose a model of a thermal network module, called a piecewise stator-housing module (PSM), that can predict the temperature of the coils in each slot of the stator. The model is then used to construct an LPTN. To verify the validity of the LPTN, coil temperature measurements are performed on three dual winding types of motors, and the results are compared with the analysis results. Finally, by assuming a case in which the brake motor is changed from normal operation to fault operation in a traffic jam, the coil-temperature analysis results of the proposed and conventional models are compared. In addition, the applications of the constructed LPTN are presented.

II. Brake System for HAD Vehicles

In vehicle systems for HAD, fault-tolerance technology is required to ensure driver safety. Some of these technologies are already being applied to electric power steering, and brake systems should enable brake performance in the event of failure. As there is minimal driver intervention in HAD, fault-tolerant systems should be able to operate without driver intervention. To address this issue, manufacturers of automobile parts are developing electronic brake systems using two controllers and two motors. An alternative to using the two motors is a dual winding motor.

A. System Configuration

Conventional brake systems amplify the force through a vacuum booster when the driver applies force to the brake pedal, as shown in Fig. 1. The amplified force generates hydraulic pressure in the master cylinder, and brake fluid is transmitted to each wheel through hydraulic lines. As shown in Fig. 2, the recently developed integrated electronic brake (IEB) is a system that replaces the vacuum booster with a motor, and

Authorized licensed use limited to: Hanyang University. Downloaded on June 22,2022 at 01:52:54 UTC from IEEE Xplore. Restrictions apply.

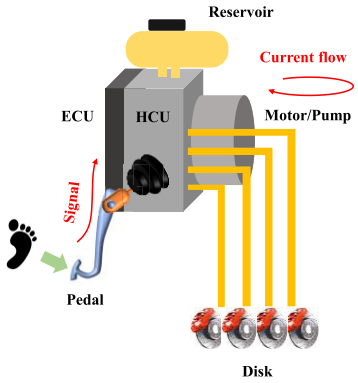

Fig. 2. Integrated electronic brake system.

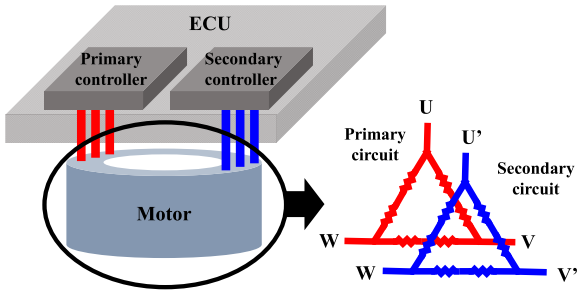

Fig. 3. Fault-tolerant winding motor.

integrates the electronic stability control (ESC) and antilock brake system (ABS) modules into one module. The system receives the pedal signal by the driver and sends it to the electronic control unit (ECU). When the motor is controlled such that current flows through the ECU, the motor converts the rotational motion into linear motion to generate pressure through the pump. In other words, when a driver applies force to the pedal, the brake pedal only generates a sensation, which is practically not related to pressure generation. Therefore, the IEB can be operated by sending an electric signal to the ECU to drive the motor and pump, even if there is no pedal operation. This indicates that the brake can work without human assistance during HAD.

In chassis products, such as steering and brake devices, fault-tolerant systems are configured to enable minimum performance manually in the event of a fault. However, if a fault occurs during HAD, the driver may be unable to control the resulting scenario quickly. As a result, an additional fault-tolerant system is required. Similarly, in the brake system, a fault-tolerant motor and ECU are needed as countermeasures against faults. Therefore, in a fault-tolerant system, the circuit of the motor is divided into two, and the circuit for controlling the motor in the ECU is divided into two, as shown in Fig. 3.

To increase the reliability of the required motor, various studies have considered the use of dual three- or six-phase machines; in the fault-tolerant brake system applied in this study, a dual three-phase method is used. When there is no fault, two controllers control the motor in the same phase; thus, the primary and secondary circuits operate normally. If one

TABLE I
CHARACTERISTICS ACCORDING TO SYMMETRIC WINDING TYPE

	LINE	POINT	ALTERNATING
NVH	△	○	◎
COST	◎	○	△
THERMAL	△	○	◎

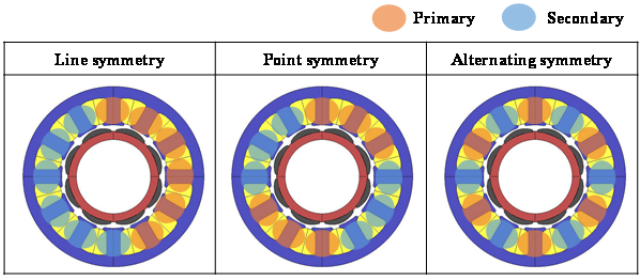

Fig. 4. Three types of fault-tolerant (dual three phase) winding motor.

of the controllers or the motor circuit fails, only one of the primary and secondary circuits works. Even when only one circuit is operated due to the failure, the motor is required to ensure system performance. In this system, the motor is designed using criteria such that problems do not occur, even if it continuously operates in the mainly used operating points during fault operation. When current flows to only one circuit of the motor in the event of a fault, to maintain the system performance, the current flow is nearly twice that in normal situations. The coil of the motor in this brake system has polyamide-imide (AIW) specifications and can be used at temperatures up to 220 $^{\circ}C$. Considering the hot spot of the coil, the maximum operating temperature is limited to within 200 $^{\circ}C$. Therefore, when designing a motor for a fault-tolerant system, the heat dissipation performance should be sufficiently considered to ensure that the temperature of the coils does not exceed the threshold within the required operating time during fault operation.

B. Fault-Tolerant Motor

In this study, the authors analyzed three types of fault-tolerant winding motors, which are called dual three-phase motors, as shown in Fig. 4. Although the winding arrangement varies according to the symmetry criterion, all the motors exhibit the same performance during normal operations. When only one of the primary and secondary circuits is operated, the torque for each motor winding type is similar; however, the three types of fault-tolerant winding motors have different characteristics in terms of the noise, vibration, and harshness (NVH), cost, and thermal behavior. As listed in Table I, with respect to NVH and thermal properties, the alternating symmetry is the most advantageous in the distribution of the force density and shows uniform loss in the windings during operation. However, the line symmetry, in which the bus bar design is not complicated, is advantageous in terms of

Authorized licensed use limited to: Hanyang University. Downloaded on June 22,2022 at 01:52:54 UTC from IEEE Xplore. Restrictions apply.

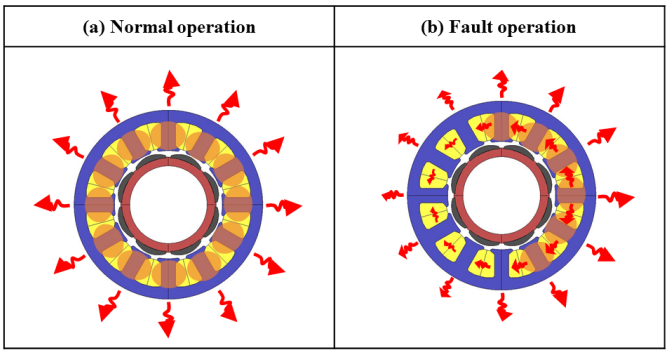

Fig. 5. Heat transfer path during (a) normal and (b) fault operations in the case of line symmetry.

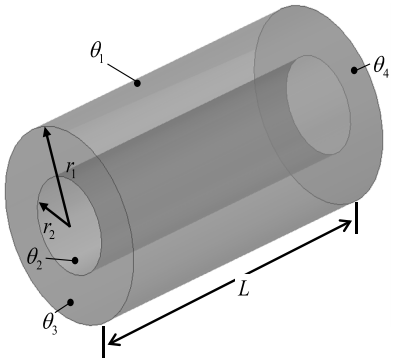

Fig. 6. Cylindrical component.

cost. Of the three methods mentioned earlier, point symmetry has intermediate characteristics. When designing a motor, as indicated, various criteria, such as NVH, cost, and temperature, may be considered. However, from a safety perspective, the thermal characteristics associated with the motor operating time are important design criteria related to size [42]–[45]. In particular, the prediction of the coil temperature is important because a large temperature difference exists between each symmetric winding in a short amount of time in which a large current flows. As a consequence, a temperature prediction program is needed. Among all the methods, the LPTN method is easy to use in the design stage of a motor because it has shorter modeling and analysis times than those of CFD and FEA. The conventional LPTN is primarily used for the prediction of the temperature during normal operation; however, in this paper, we propose a method to calculate the temperature even if only one circuit (primary or secondary) is operated in the dual three-phase winding motor, as shown in Fig. 4.

III. LPTN With Piecewise Stator-Housing Modules

This paper proposes a PSM with thermal resistance that includes a coil, insulator, stator core, and housing. As shown in Fig. 5(a), during normal operation, the same current flows through each coil of the stator, and thus the losses generated in the coils of each slot are the same. Therefore, the temperature of each coil is the same, and heat is transferred only in the axial and radial directions. Conventional LPTNs focus mainly on normal operations and consider heat transfer in the radial and axial directions, but not in the tangential direction. However, as shown in Fig. 5(b), if only the primary circuit operates during a fault, no current flows through the secondary coil. As such, the coil temperature increases due to the copper or core loss of the primary circuit, and heat is transferred from the high- to the low-temperature region. Thus, the heat generated in the primary circuit is transferred to the secondary circuit, and escapes through the motor housing. Fig. 5(b) shows the heat-transfer path when only the primary circuit is operated in the case of line symmetry winding type. Because heat is transmitted not only in the radial and axial directions but also the tangential direction, a thermal-resistance model that considers the heat transfer in the tangential direction is required. Therefore, the thermal-resistance model for each slot should be independent in order to express the phenomenon where the heat is transferred from the working slot to the non-working slot according to the winding type, as is the case with only the primary circuit working in Fig. 4.

A. Basic Theory of LPTN

The lumped thermal model was proposed by Mellor [25]. In [25], the thermal resistance of each component of the induction motor was described in detail as a cylindrical model. The thermal resistance of each motor component in the axial and radial directions were expressed using equations. In addition, the heat flow can be intuitively determined by representing the connection of each component as a circuit [25]. In subsequent studies, based on the previously proposed cylindrical model, a thermal equivalent circuit for an interior permanent magnet (IPM) model was proposed [26]. In [26], the stator has three-phase concentrated windings, and the rotor is a single-layer IPM rotor structure, which is different from induction machine by Mellor. In order to use cylindrical model proposed by Mellor, the rectangular magnet in the rotor was equivalently changed to a cylindrical model in [26]. In this paper, based on [25] and [26], the LPTN of a surface-mounted permanent magnet synchronous motor (SPMSM) used as a brake motor is constructed. The basic thermal-resistance calculation method is based on the cylindrical component, as shown in Fig. 6, where θ_1 and θ_2 are the temperatures of the outer and inner diameters of the cylinder, respectively, and θ_3 and θ_4 are the temperatures of the front and rear surfaces of the cylinder, respectively. The thermal resistance of the cylinder is shown in Fig. 7, where θ_m is the average temperature of the cylinder, u represents the internal heat generation, and C is the thermal capacitance [25]. R_{1a} and R_{2a} are the axial heat resistances at the center of the cylinder, R_{1r} and R_{2r} are the radial heat resistances of the inner and outer diameters of the cylinder, respectively, and R_{3a} and R_{3r} are thermal resistances that compensate the maximum temperature in the axial and radial directions with the average temperature.

Each equation of the cylindrical component consists of the axial and radial thermal conductivities (k_{lr} and k_{la}, respectively) and the geometry information of the cylinder according

Authorized licensed use limited to: Hanyang University. Downloaded on June 22,2022 at 01:52:54 UTC from IEEE Xplore. Restrictions apply.

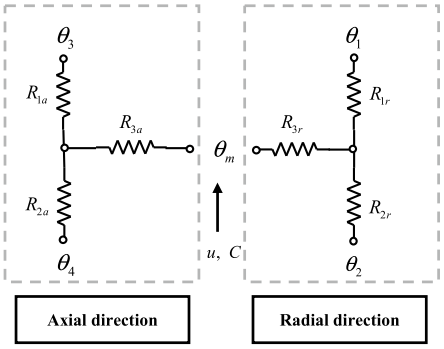

Fig. 7. Axial and radial thermal networks.

to the following expressions.

$$R_{1r} = \frac{1}{4\pi k_{lr} L}\left[1 - \frac{2r_2^2 \ln\left(\frac{r_1}{r_2}\right)}{(r_1^2 - r_2^2)}\right] \tag{1}$$

$$R_{2r} = \frac{1}{4\pi k_{lr} L}\left[\frac{2r_1^2 \ln\left(\frac{r_1}{r_2}\right)}{(r_1^2 - r_2^2)} - 1\right] \tag{2}$$

$$R_{3r} = \frac{-1}{8\pi (r_1^2 - r_2^2) k_{lr} L}\left[r_1^2 + r_2^2 - \frac{4r_1^2 r_2^2 \ln\left(\frac{r_1}{r_2}\right)}{(r_1^2 - r_2^2)}\right] \tag{3}$$

$$R_{1a} = \frac{L}{2\pi k_{la}(r_1^2 - r_2^2)} \tag{4}$$

$$R_{2a} = \frac{L}{2\pi k_{la}(r_1^2 - r_2^2)} \tag{5}$$

$$R_{3a} = \frac{-L}{6\pi k_{la}(r_1^2 - r_2^2)} \tag{6}$$

$$C = c\rho\pi L(r_1^2 - r_2^2) \tag{7}$$

B. Piecewise Stator-Housing Modules (PSMs)

In the proposed model, the tangential heat-resistance component was added to the basic cylindrical heat-resistance model. Fig. 8 shows the partial model of the entire cylinder divided by n slots. The red resistors in Fig. 8 are the thermal resistances for heat transfer to the left and right in the case of a temperature difference for each of the n models. To calculate the left and right thermal resistances, the geometric mean distance was considered. The general resistance equation of the *1/n* cylindrical component model is as follows:

$$R_{1r} = \frac{360}{4\pi k_{lr} L\phi}\left[\frac{2r_1^2 \ln\left(\frac{r_1}{r_2}\right)}{r_1^2 - r_2^2} - 1\right] \tag{8}$$

$$R_{2r} = \frac{360}{4\pi k_{lr} L\phi}\left[1 - \frac{2r_2^2 \ln\left(\frac{r_1}{r_2}\right)}{r_1^2 - r_2^2}\right] \tag{9}$$

$$R_{3r} = \frac{-360}{8\pi k_{lr} L\phi (r_1^2 - r_2^2)}\left[r_1^2 + r_2^2 - \frac{4r_1^2 r_2^2 \ln\left(\frac{r_1}{r_2}\right)}{r_1^2 - r_2^2}\right] \tag{10}$$

$$R_{1a} = \frac{360L}{2\pi k_{la}(r_1^2 - r_2^2)\phi} \tag{11}$$

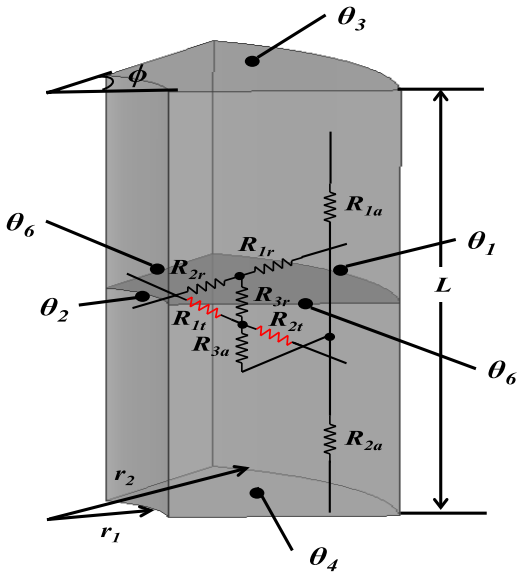

Fig. 8. Diagram of 1/n model of the cylindrical component in the PSM.

$$R_{2a} = \frac{360L}{2\pi k_{la}(r_1^2 - r_2^2)\phi} \tag{12}$$

$$R_{3a} = \frac{-360L}{6\pi k_{la}(r_1^2 - r_2^2)\phi} \tag{13}$$

$$R_{1t} = \frac{\pi \cdot \phi \cdot e^{\frac{r_1^2 \ln r_1 - r_2^2 \ln r_2}{r_1^2 - r_2^2} - \frac{1}{2}}}{k_{lr} \cdot L \cdot (r_1 - r_2) \cdot 360} \tag{14}$$

$$R_{2t} = \frac{\pi \cdot \phi \cdot e^{\frac{r_1^2 \ln r_1 - r_2^2 \ln r_2}{r_1^2 - r_2^2} - \frac{1}{2}}}{k_{lr} \cdot L \cdot (r_1 - r_2) \cdot 360} \tag{15}$$

$$C = \frac{c\rho\pi L(r_1^2 - r_2^2)\phi}{360} \tag{16}$$

The meaning of each parameter in the equation is the same as the cylindrical component mentioned earlier, and ϕ is the angle that corresponds to one slot. For example, in the case of 12 slots, if the angle of one slot is 30°, $\phi = 30$. The axial thermal conductivity (k_{la}) is much lower than the radial thermal conductivity (k_{lr}) because of the thin insulation layers between the electrical steel sheets. In (14) and (15), the thermal conductivity in the tangential direction is the same as the thermal conductivity in the radial direction. This is because the material is the same in the radial and tangential directions of heat conduction, unlike the axial directions. Fig. 9 shows the thermal network of the cylindrical model considering the tangential direction. The thermal-resistance model for one slot is configured as shown in Fig. 10, and comprises the housing, stator core, insulator, and coil. The target electric motor is a concentrated winding model, and was considered for use in the thermal equivalent circuit. For this, the left and right coils in the thermal equivalent circuit are connected through the end windings (R5-4-1, R5-4-2, R'5-4-1, and R'5-4-2). The PSM is represented as a total of 10 nodes outside the stator resistance module, and these nodes can be connected to each other. In Fig. 10, (a) is the node from which heat escapes

Authorized licensed use limited to: Hanyang University. Downloaded on June 22,2022 at 01:52:54 UTC from IEEE Xplore. Restrictions apply.

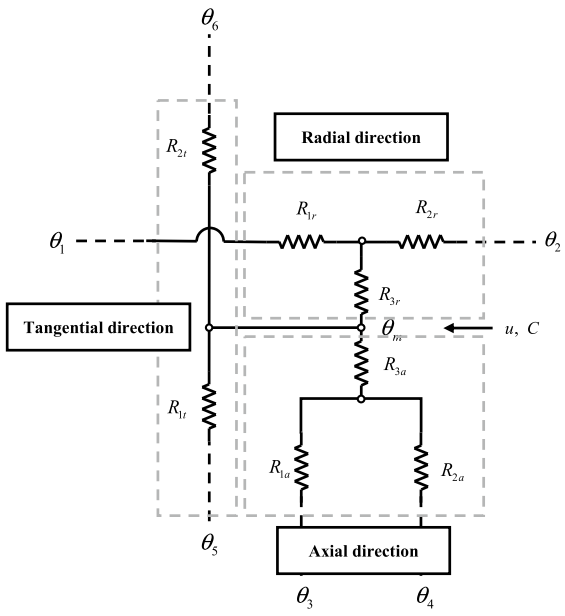

Fig. 9. Axial, radial, and tangential thermal networks in PSM.

from the housing to the outside air, (b) and (b)' denote the nodes from which heat is transferred to the left and right sides of the other slot housing, (c) and (c)' denote the nodes from which heat is transferred to the left and right sides of the other slot stator yoke from the stator yoke, (d) represents the node from which heat is transferred from the teeth and coil to the air gap, (e) and (e)' represent the same node from which the heat is transferred to the front cover, and (f) and (f)' represent the same node from which heat is transferred to the rear cover. Although (e) and (e)' as well as (f) and (f)' indicate only two nodes, they are represented by four nodes to facilitate the connection between the stator resistance modules. Each node in a stator module encounters a node in either slot.

C. Proposed LPTN and Heat-Transfer Coefficients

Fig. 11 shows the thermal network of the motor based on the PSM. Each PSM is connected in parallel according to the number of slots. For example, if the motor is configured with 12 slots, 12 corresponding PSMs are connected in parallel in the LPTN. However, the rotor does not consist of a parallel network module because it is assumed that the rotor rotates, and thus the temperature of the air gap adjacent to the rotor surface is constant along the mechanical angle. Each circuit parameter of the PSM is determined based on the dimensions of the motor and thermal properties of the material for each component. For example, for the cylindrical model, r_1, r_2, L, etc., represent the dimensions, and c, ρ, k, etc., are determined depending on the material of the motor component. Additionally, the rotor shown in Fig. 11 is an SPM type with a hollow shaft assembled, and its thermal resistances and their compositions have been modified based on the equations in previous papers [25], [26]. In the conventional LPTN, as shown in Fig. 12 (a), the thermal networks of the stator and housing are not divided into slots. Therefore, the temperature can be predicted only in the normal operating or the non-operating state in which current in all slots flows or not. However, in the proposed LPTN, the thermal resistance network is separated for each slot and connected in parallel as shown in Fig. 12(b), thus it is possible to select an operation mode for each slot. Therefore, it enables temperature analysis when only one of the two circuits is operated in a dual winding motor.

In the case of LPTN, the accuracy of the thermal analysis varies depending on the heat-transfer coefficients. This study defines ambiguous heat-transfer coefficients as undetermined parameters that are to be determined by the optimization process explained at the end of this section. The heat-transfer coefficients were calculated by optimizing the test results and simulation results under normal operation. This optimization compensates for errors that can only be caused by the test environment and simplified modeling. The use of the optimized heat-transfer coefficients in the same test environment and motor is valid for verification of the proposed LPTN under the same test conditions with the same motor. Before conducting the optimization process, brief explanations and boundaries of the ambiguous heat-transfer coefficients are first presented. The ambiguous heat-transfer coefficients considered in this study are the convective heat-transfer coefficients, conductivity, and contact thermal-resistance coefficient.

The convective heat-transfer coefficient depends on the fluid state and surface shape on which convection occurs. Convection of the motor mainly occurs outside the motor housing, in the air gap and in the end space between the active parts of the motor and the housing end cover. In particular, for the end-air region, the convective heat-transfer coefficients of the stator and rotor ends are separately defined because of the rotating state of the rotor. For the convective heat-transfer coefficient outside the motor housing, Staton and Cavagnino [29] Cengel and Ghajar [34] described the heat-transfer coefficients during natural and forced convection, respectively. As the air outside the motor housing during testing transfers heat through natural convection, the coefficient is correlated with the lower and upper boundaries of the coefficient corresponding to natural convection. In addition, the air in the air gap transfers heat through forced convection based on the Taylor vortex between the stationary cylinder, which is the inner stator, and the rotary cylinder, which is the outer rotor. Furthermore, heat convection from the rotor end to the end space is considered as forced convection of the rotary disk. Previous studies have investigated forced convection in the airgap and rotor end of rotating electrical machines [35]–[37]. Based on the results of these studies, the upper and lower boundaries in this study were set during the optimization of the test results. Finally, the convection from the stator end to end-air region was considered as mixed natural–forced convection because the rotation of the rotor causes the air in the stator end to flow. Therefore, the lower and upper boundaries of the convective heat-transfer coefficient in this region were set based on [38] and [39].

As heat conduction occurs in all parts of the motor, the thermal conductivity of the material is important for thermal analysis. However, there is some degree of complexity when determining the thermal conductivity of specific parts, namely

Authorized licensed use limited to: Hanyang University. Downloaded on June 22,2022 at 01:52:54 UTC from IEEE Xplore. Restrictions apply.

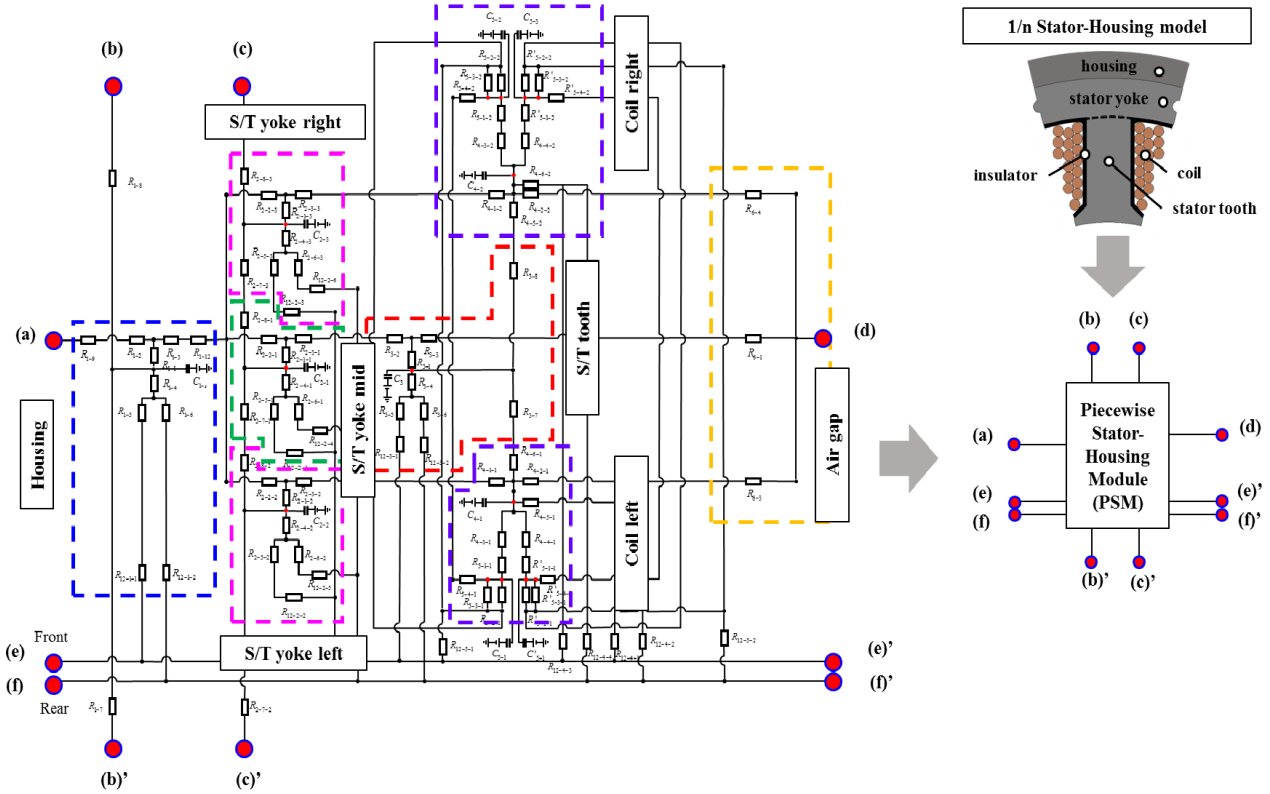

Fig. 10. PSM thermal networks.

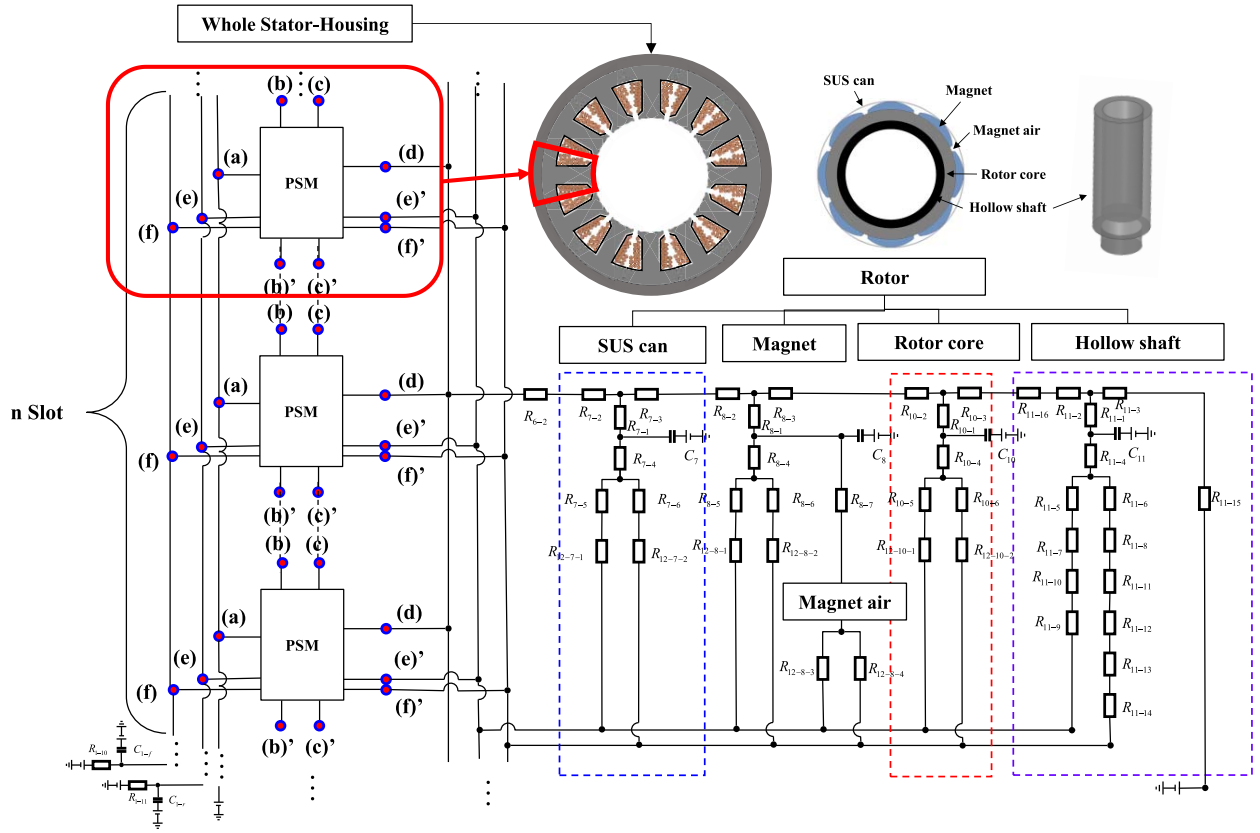

Fig. 11. LPTN of PMSM using PSM.

the winding and the stacked core. First, the winding consists of various materials, such as copper, thin layers of coating for each conductor (e.g., polyamide), and the vacancy or insulation between round conductors. Therefore, determining the thermal conductivity of the winding is difficult. As such, according to [33] and [39], the conductivity of the winding is correlated

Authorized licensed use limited to: Hanyang University. Downloaded on June 22,2022 at 01:52:54 UTC from IEEE Xplore. Restrictions apply.

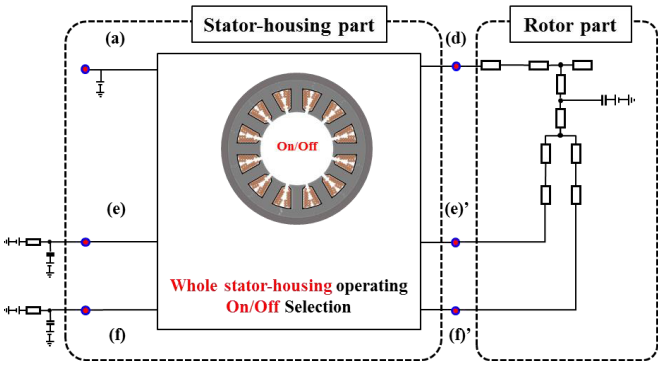

(a) Concept of conventional LPTN.

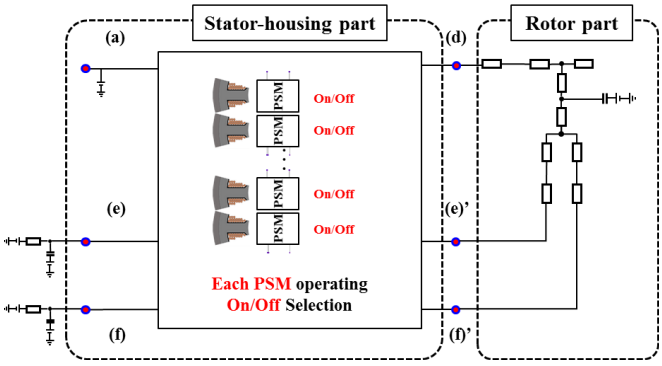

(b) Concept of proposed LPTN

Fig. 12. Difference in concept of the conventional and proposed LPTN.

TABLE II
UNDETERMINED PARAMETERS FOR PROPOSED LPTN

	Items	Unit	Boundary Lower	Boundary Upper	Value
X1	Ambient convective heat-transfer coefficient	W/m^2·°C	5	50	6.944
X2	Housing-stator contact thermal-resistance coefficient	W/m^2·°C	1000	6000	5976
X3	Lamination axial conductivity	W/m^2·°C	0.2	0.5	0.452
X4	Radial conductivity factor	-	0.2	1.5	0.697
X5	Airgap convective heat-transfer coefficient	W/m^2·°C	50	120	119.9
X6	Shaft-core contact thermal-resistance coefficient	W/m^2·°C	500	6000	526.6
X7	Shaft inner convective heat-transfer coefficient	W/m^2·°C	15	100	15.26
X8	Stator end convective heat-transfer coefficient	W/m^2·°C	20	120	20.29
X9	Rotor end convective heat-transfer coefficient	W/m^2·°C	20	120	119.5

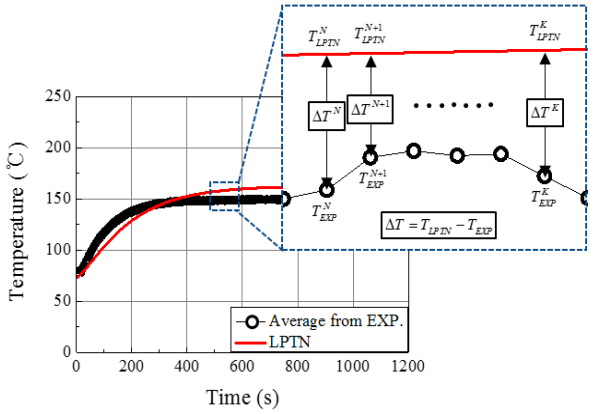

Fig. 13. Definition of objective function.

with the optimization with the boundaries based on previous studies. Moreover, the radial and axial thermal conductivities of the stacked core differ from each other because of their lamination. The radial thermal conductivity can be similar to the thermal conductivity of the electrical steel sheet material; however, the axial thermal conductivity is much lower than the radial thermal conductivity because of the thin insulation layers between the electrical steel sheets. Thus, the axial thermal conductivity of the core is selected as a parameter to be determined through optimization.

When heat is transferred between two solid materials, a tiny interference gap due to the non-ideal contact state complicates the heat transfer. This phenomenon results in a temperature difference between the two contacting surfaces. Therefore, the contact thermal-resistance coefficient, with the same unit as the convective heat-transfer coefficient, is considered as a parameter. The contact states of the motor's housing stator and shaft core are reflected, and their boundaries are set according to the studies conducted by Simpson *et al.* [40] and Camilleri *et al.* [41].

For the case with no fan or with very low motor speeds, radiation heat transfer should be considered. Boglietti *et al.* [31] proposed radiation heat-transfer coefficients using vacuum tests. However, because the radiation heat transfer is incorporated in the convective heat transfer coefficient mentioned earlier, it is not considered as a resistance coefficient in the proposed LPTN. With the exception of the deterministic parameters, the undetermined parameters and their feasible boundaries are listed in Table II.

In this study, these undetermined parameters were determined by adopting an optimization process. Before parameter determination, the objective function was formulated as follows, as shown in Fig. 13:

$$f = \sum_{K=1}^{END} \left(\Delta T\_\text{end\_coil}^{K}\right)^2 \tag{17}$$

Consequently, the parameters that determine the problem formulation are organized as follows:

$$\begin{aligned} &\text{Find} && \text{X1, X2, X3, X4, X5, X6, X7, X8, X9} \\ &\text{To minimize} && f \\ &\text{Subject to} && 5 < \text{X1} < 50,\quad 1000 < \text{X2} < 6000, \\ & && 0.2 < \text{X3} < 0.5,\quad 0.2 < \text{X4} < 1.5, \\ & && 50 < \text{X5} < 120,\quad 500 < \text{X6} < 6000, \\ & && 15 < \text{X7} < 100,\quad 20 < \text{X8} < 120, \\ & && 20 < \text{X9} < 120,\quad \text{X8} < \text{X9},\quad \text{X9} < \text{X5} \end{aligned}$$

Next, the design of experiment (DOE) was conducted using Latin hypercube sampling. The number of experiments was

Authorized licensed use limited to: Hanyang University. Downloaded on June 22,2022 at 01:52:54 UTC from IEEE Xplore. Restrictions apply.

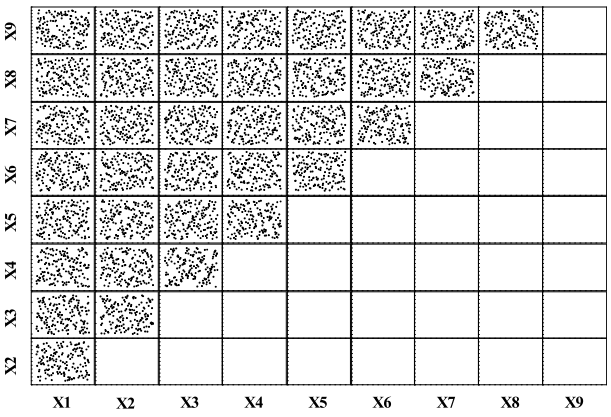

Fig. 14. Design of experimental result based on Latin hypercube sampling.

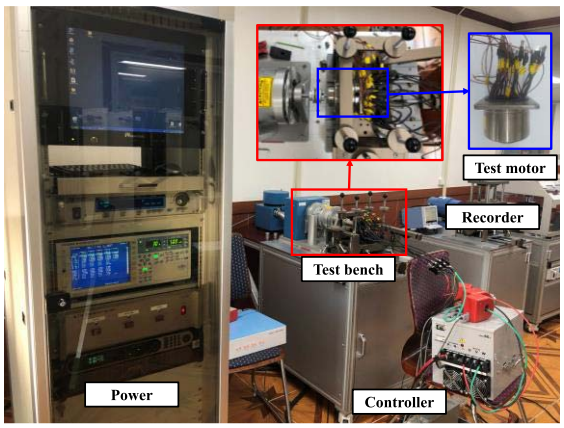

Fig. 15. Thermal test environment.

set to 90, i.e., 10 experiments were conducted for each variable [46]. Fig. 14 shows the DOE result, which has a discrepancy of 0.01. The discrepancy is one of the measurements of space-filling design [47], [48]. The value of 0.01 was determined based on the tendency of space-filling improvement according to the number of samples. Based on this result, the surrogate model of the objective function was generated by modeling the Gaussian process. The objective function was set to minimize the temperature difference for both transient and steady state temperature. Finally, optimization was conducted using the gradient-based optimization algorithm, and the undetermined parameters are listed in the "Value" column of Table II.

IV. Verification Results

This section presents the verification of LPTN using PSM during normal and fault operation modes according to the current level. In addition, in the fault operation, three dual winding types were tested, and the results were compared with the analyzed values. Moreover, the usefulness of the proposed LPTN was proved by comparing the analyzed values of the conventional and proposed LPTNs.

A. Experimental Setup

Herein, we compare the analysis results obtained using the LPTN with PSM with the test results. Generally, the temperature is measured by attaching a thermocouple to the winding of the motor. To measure the temperature of all the coils of the slot, thermocouples were attached to the top of the end windings of the 12slots. Even if the thermocouple is attached to the same point of the same designed motors, a temperature deviation could occur depending on the state of the attachment of the thermocouple and the manufacturing tolerance. To overcome the errors caused by these factors, temperature comparison tests of the line, point, and alternating symmetries were conducted using one motor sample. To measure the temperature according to the winding symmetry using one sample, a terminal was connected to the coil in each slot, as shown in the expanded view of the test motor in Fig. 15. For temperature measurement, t-type thermocouple wire that can measure temperatures up to 260 $^{\circ}C$ and YOKOGAWA's MV 100 recorder (12 channels) were used. Next, the terminal was connected to the bus bar according to the winding method (Fig. 16). In Fig. 16, to distinguish between the working slot and non-working slot, the working slots are colored in light red, and the non-working slots are colored in light blue. First, as shown in Fig. 16 (a), the temperature of the 12 coils was measured under normal operation (both the primary and secondary circuits were driven). In this test, the temperature of coil 3 was the highest under the same operating conditions, and thus coil 3 was selected as the hot spot. The connection of the bus bar was changed for each winding type during the fault operation to record the highest temperature in the same coil (coil 3). As a result, as shown in Fig. 16(b)–(d), in the case of line symmetry, the current in the W phase flows in the hot spot, while in the case of point and alternating symmetries, the current in the V phase flows to the hot spot. The test was conducted at 23 $^{\circ}C$. If the current condition changed, the motor was cooled sufficiently before the next test. Fig. 15 describes the test environment. The range of use of the coil is up to 220 $^{\circ}C$. However, when the temperature of the coil increased and was close to 180 $^{\circ}C$, the test was stopped for safety.

B. LPTN Verification Under Normal and Fault Operations

As mentioned above, the temperature difference of the coil for each slot occurs according to the degree of thermocouple attachment, the motor manufacturing tolerance, and the test environment. Thus, when comparing the analysis results and the test results, the average test temperature of the coils of the group that have the same temperature under ideal conditions is used as the test results. Fig. 17 shows the temperature difference between the test and simulation results with optimized heat-transfer coefficients using the PSM during normal operation (Fig. 16(a)). Under normal operation, even in the LPTN using the PSM, heat is not transferred in the tangential direction because the components of each PSM have the same temperature. In other words, even if the LPTN using a PSM is used, the result is the same as that of a conventional LPTN if there is no heat transfer in the tangential direction in the case of normal operation. The test and simulation results using the LPTN with PSM were compared according to the current value. The analysis results with optimized heat transfer

Authorized licensed use limited to: Hanyang University. Downloaded on June 22,2022 at 01:52:54 UTC from IEEE Xplore. Restrictions apply.

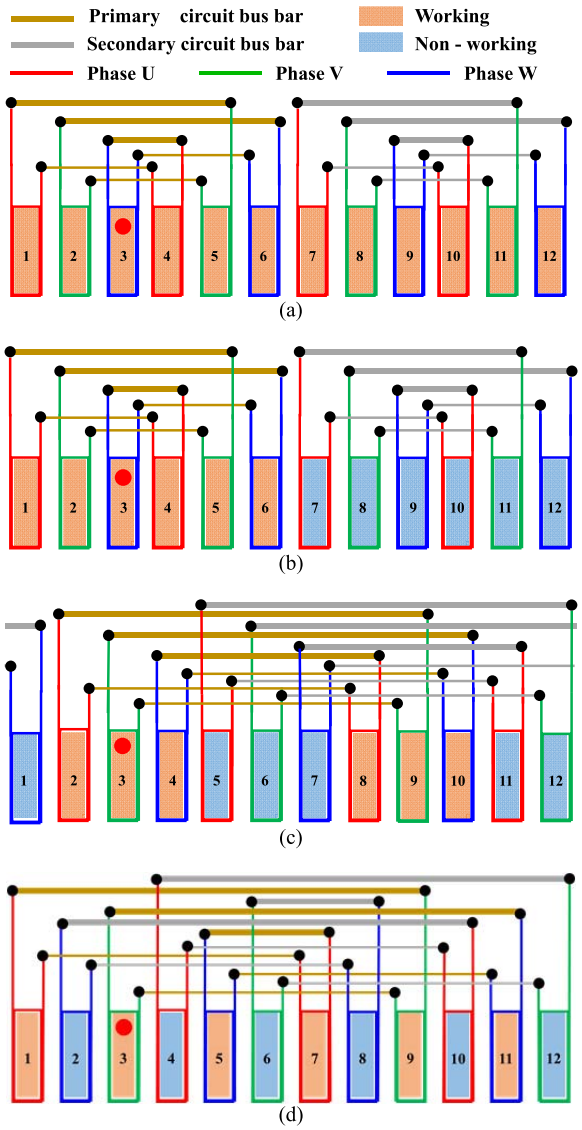

Fig. 16. Winding connection during normal and fault operations in the experiment. (a) Normal operation, (b) line symmetry during fault operation, (c) point symmetry during fault operation, and (d) alternating symmetry during fault operation.

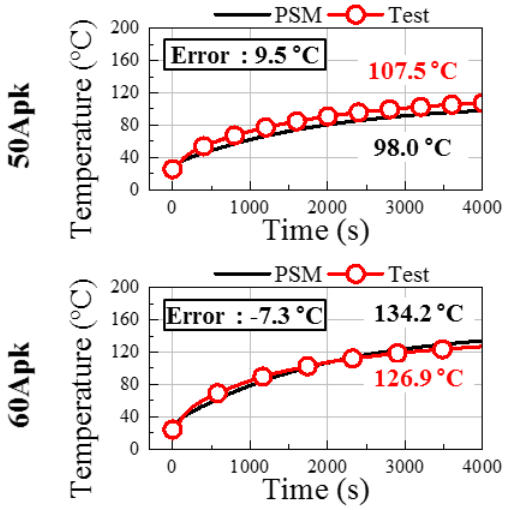

Fig. 17. Test and simulation results obtained during normal operation.

coefficients and test results obtained for each current value are in close agreement, with an error of 10 $^{\circ}C$. Therefore, the heat-transfer coefficient values listed in Table II, which are determined through surrogate model-based optimization, are valid. To increase the reliability of the proposed model (LPTN with PSM) considering the heat transfer in the tangential directions, six cases were compared according to the current value and symmetric winding type under fault operation in which heat transfer occurs in the tangential direction. For analysis, the optimized heat-transfer coefficient during normal operation was used for the following reasons. First, since the tested motor is a closed motor, we assumed that coefficients related to convective heat transfer among the optimized values (i.e., X5, X7 and X8) do not change significantly according to the operation mode. Second, the heat transfer between the operating coil and the non-operating coil during a fault occurs mainly through conduction, and the thermal conductivity in the tangential direction of the core, which is the main heat-transfer path, is a known value. For example, the heat from the operating coil is transferred to its stator core. The heat is transferred to the non-operating adjacent stator core and then to the coil corresponding to the non-operating stator core. In addition, optimized parameters related to conduction (X2 and X6) are parameters determined by mechanical factors, and thus they were judged to not be changed by the test conditions. Although a resultant error may occur, it is possible to determine the suitability of the model. To confirm the accuracy in transient and steady states, 20 and 100 A_{pk} currents were applied, as shown in Fig. 18. Depending on the type of symmetry, the coils that should have the same temperature in ideal conditions were grouped together. In the analysis, the coils in each group had the same temperature. For example, as shown in Fig. 16(b), the temperatures of the coils (3, 4), (2, 5), and (1, 6) are grouped. As indicated inn Fig. 16(c), the temperatures of the coils (3, 9) and (2, 4, 8, 10) are grouped. Fig. 16(d) shows that the temperatures of the coils (1, 3, 5, 7, 9, 11) form a group.

Fig. 18 shows the results obtained by comparing the analysis and test values of the coil temperature according to the winding type during fault operation. The measured coil temperature has a difference within 5-10 $^{\circ}C$ in each group, and thus the average temperature in each group is used for ease of comparison with the analysis results, as mentioned above. The test and analysis results are compared according to the winding type, coil position, and current. In Fig. 18, the red solid line with white dots is the test result, and the black solid line is the analysis result. The tables show the temperature and error for the simulation and test at the same end of the time. The temperature error values at 100 and 20 A_{pk} in the table are similar. In the steady state when a 20 A_{pk} current was applied, the highest temperature among the test and the analysis values was in the order of line > point > alternating symmetry, and the lowest temperature was in the order of line < point < alternating symmetry. However, the temperature did

Authorized licensed use limited to: Hanyang University. Downloaded on June 22,2022 at 01:52:54 UTC from IEEE Xplore. Restrictions apply.

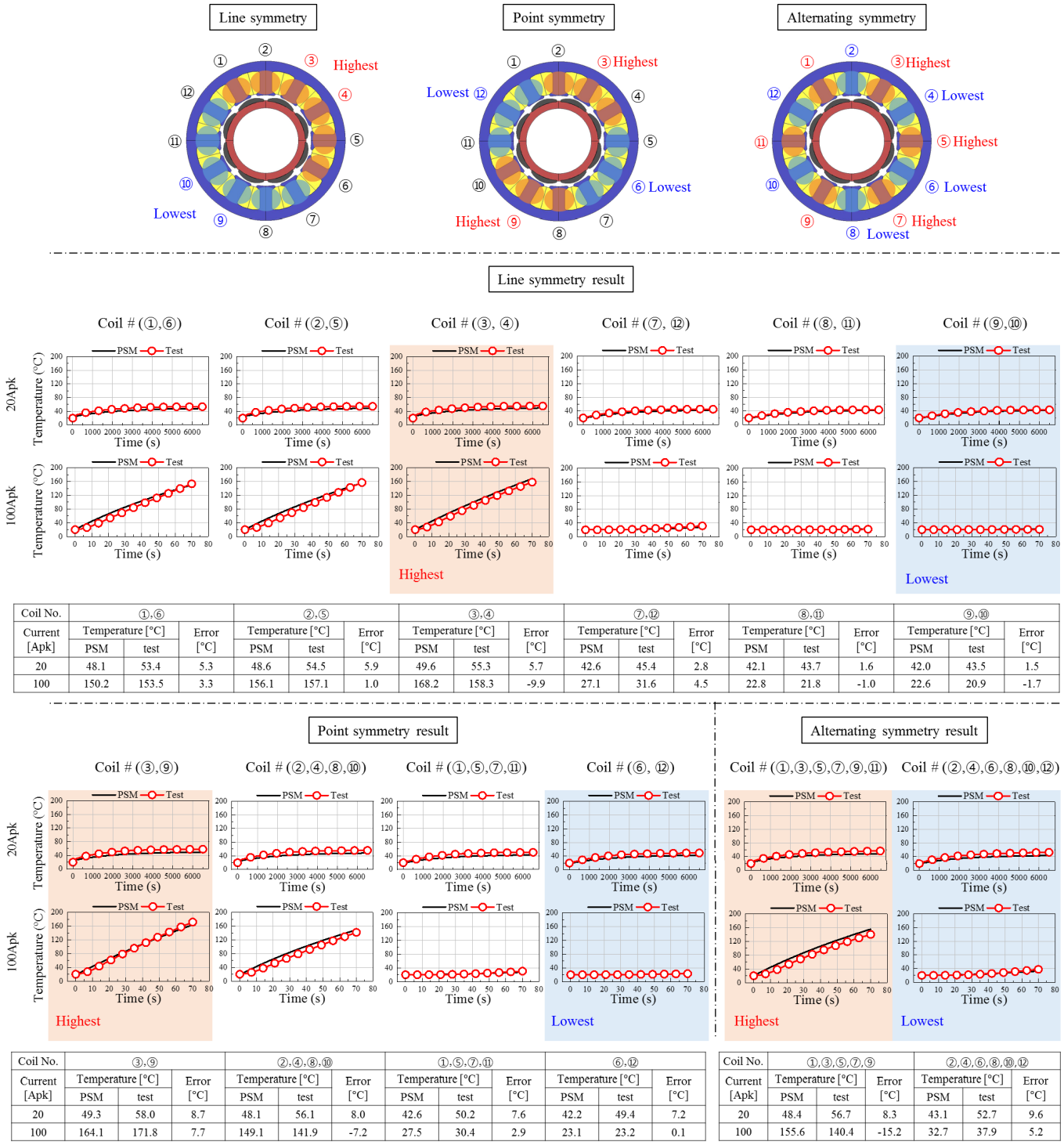

Coil No.	①,⑥			②,⑤			③,④			⑦,⑫			⑧,⑪			⑨,⑩		
Current [Apk]	Temperature [°C]		Error [°C]	Temperature [°C]		Error [°C]	Temperature [°C]		Error [°C]	Temperature [°C]		Error [°C]	Temperature [°C]		Error [°C]	Temperature [°C]		Error [°C]
	PSM	test		PSM	test		PSM	test		PSM	test		PSM	test		PSM	test	
20	48.1	53.4	5.3	48.6	54.5	5.9	49.6	55.3	5.7	42.6	45.4	2.8	42.1	43.7	1.6	42.0	43.5	1.5
100	150.2	153.5	3.3	156.1	157.1	1.0	168.2	158.3	-9.9	27.1	31.6	4.5	22.8	21.8	-1.0	22.6	20.9	-1.7

Coil No.	③,⑨			②,④,⑧,⑩			①,⑤,⑦,⑪			⑥,⑫		
Current [Apk]	Temperature [°C]		Error [°C]	Temperature [°C]		Error [°C]	Temperature [°C]		Error [°C]	Temperature [°C]		Error [°C]
	PSM	test		PSM	test		PSM	test		PSM	test	
20	49.3	58.0	8.7	48.1	56.1	8.0	42.6	50.2	7.6	42.2	49.4	7.2
100	164.1	171.8	7.7	149.1	141.9	-7.2	27.5	30.4	2.9	23.1	23.2	0.1

Coil No.	①,③,⑤,⑦,⑨			②,④,⑥,⑧,⑩,⑫		
Current [Apk]	Temperature [°C]		Error [°C]	Temperature [°C]		Error [°C]
	PSM	test		PSM	test	
20	48.4	56.7	8.3	43.1	52.7	9.6
100	155.6	140.4	-15.2	32.7	37.9	5.2

Fig. 18. Comparison of test and simulation results obtained using the LPTN with PSM according to the symmetric winding type and current at different coil positions during fault operation.

not vary significantly depending on the winding type and coil positions. In the case of a transient state in which a 100 A_{pk} current was applied, the temperature difference varied greatly depending on the coil position within the same operating time, but the order of the highest and lowest temperatures according to the winding type is the same as that for 20 A_{pk}. As mentioned earlier, heat transfer occurs mostly through conduction insidethe motor, and the time delay is caused by the thermal capacitance of each component constituting the PSM until the heat generated from the operating PSM is transferred to the non-operating PSM. For example, in the line symmetry result, the temperature for each coil position under 20 A_{pk} is similar. This is because there was enough time for heat to be transferred to each PSM before the coil temperature reached the usage limit. However, the difference between the highest and lowest temperatures is large in the transient state in which a 100 A_{pk} current is applied. This is because the coil temperature of the operating PSM reaches the usage limit

Authorized licensed use limited to: Hanyang University. Downloaded on June 22,2022 at 01:52:54 UTC from IEEE Xplore. Restrictions apply.

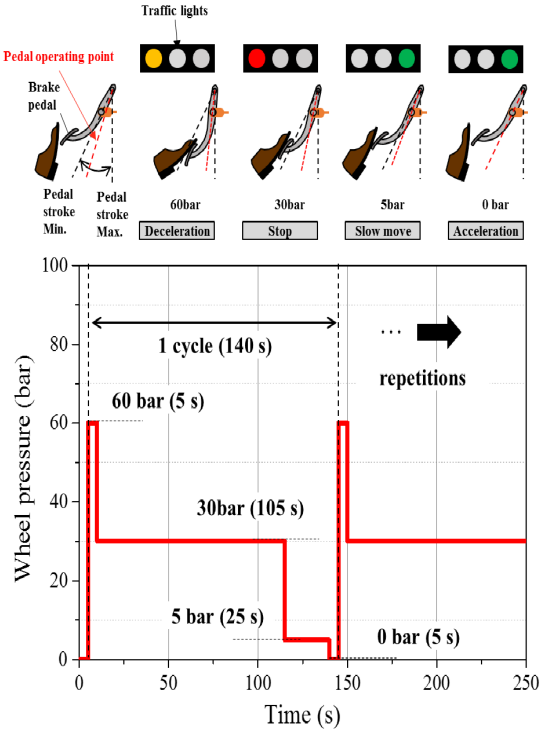

Fig. 19. Virtual wheel pressure pattern in a traffic jam at four-legged downhill intersections.

within a short period of time, and thus there is insufficient time for the heat generated from the operating PSM to be transferred to the non-operating PSM. As both results are similar under all conditions, the proposed LPTN model using PSM is valid. The error is considered to be caused by the fact that the contact resistance between the stator core segments is not reflected, and the convective heat-transfer coefficient is treated as a constant which is optimized under normal operation conditions. The error is also caused by measurement errors.

C. Temperature Estimation in Virtual Traffic Jam

In a brake system with a line symmetry motor considering HAD, the estimated coil temperature result of the motor with conventional LPTN is compared with the proposed LPTN with PSM, assuming the primary circuit failure of the motor occurs during normal brake operation. The proposed LPTN is assumed to be valid for any current condition or pattern because the test and simulation results for each current, winding type, steady state and transient state were compared as shown in Fig. 17 and 18 [49], [50]. In the analysis of the conventional LPTN, the same proposed LPTN is used. However, the current was applied to all PSMs of the proposed LPTN to prevent heat transfer in the tangential direction. Therefore, the results are the same as those of the conventional LPTN analysis.

For temperature prediction in virtual traffic jam, the virtual traffic jam pattern is defined similar to that of the traffic conditions at four-legged downhill intersections. As shown in Fig. 19, a driver starts decelerating the car for 5 *s* at a

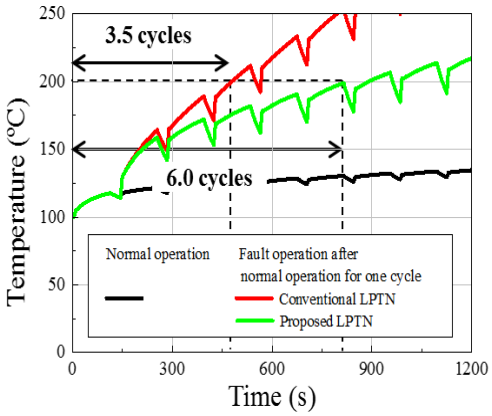

Fig. 20. Coil temperature estimation using proposed and conventional LPTNs.

yellow traffic light with a wheel pressure of 60 *bar*, and stops the car for 105 *s* at a red traffic light. When the traffic light turns green, the car moves slowly for 25 *s* while maintaining a wheel pressure of 5 *bar* due to traffic jam. After 25 *s*, the driver releases the brake pedal for 5 *s* to accelerate the car. In other words, the time required for the car to move on the road in each direction is 35 *s*. Consequently, the period of traffic signal in each direction is 140 *s*, including stop and movement time. In the case of a traffic jam, it is assumed that the period pattern of 140 *s* is repeated four times and then passed through an intersection. It means that at least four repetitive actuation patterns of the brake are required by the driver. In addition, we assumed that one circuit of the motor or ECU fails after one cycle of normal driving, as shown in Fig. 20. Therefore, after one cycle, twice the amount of current is applied to the motor to create the same pressure by using one circuit. Assuming that the vehicle was driven before entering the intersections, the initial temperature of the motor coil is set to 100 °*C* and the temperature inside the engine room is set to 80 °*C* for the simulation.

When the temperature of the motor coil is below 200 °C, the brake can operate for up to three point five and six cycles when using the conventional and proposed LPTNs, respectively, as shown in Fig. 20. The difference in the number of cycles is that the conventional LPTN does not consider the heat transfer in the tangential direction; thus, heat accumulates continuously in the coil. In contrast, in the proposed LPTN, the generated heat is transferred in the tangential direction, and thus accumulation and dissipation occur simultaneously.

This temperature characteristic is crucial in the motor design as it is necessary to increase or decrease the copper loss of the motor to satisfy the temperature characteristic. This can be achieved by changing the current density per unit torque. Eventually, the change in the current density leads to a change in the diameter of the coil, which ultimately results in a change in the outer diameter or stack length of the motor. As shown in Fig. 19, if four repetitions are required in the case of a traffic jam, the results of the analysis using conventional LPTN do not meet the requirement, and the designed motor is judged to overheat. Therefore, the motor must be designed

Authorized licensed use limited to: Hanyang University. Downloaded on June 22,2022 at 01:52:54 UTC from IEEE Xplore. Restrictions apply.

largely to satisfy the temperature condition. However, when the proposed LPTN is used, it is possible to design a motor with a reduced size because the performance exceeds the required specification. Therefore, the proposed LPTN using PSMs is useful in motor design by making it possible to predict the motor temperature more accurately than in conventional LPTN during fault operation in fault-tolerant systems. Moreover, when the proposed LPTN is applied to brake overheating protection (OHP) logic control, the performance of the brake is not degraded owing to accurate temperature prediction in the event of a fault, thereby improving driver safety.

V. Conclusion

In this paper, we proposed an LPTN using a PSM that is capable of predicting the temperature of a motor coil in which the heat transfer in the tangential direction is considered when analyzing fault driving in a fault-tolerant brake system in the case of HAD. The heat-transfer coefficient value was calculated by performing optimization using the surrogate model based on the results obtained under normal operation. The proposed LPTN using PSMs was verified by comparing the test and simulation results for each winding type when the motor is in fault operation mode. Finally, by assuming a traffic jam scenario, when there is a fault condition during brake operation, the temperature difference between the analysis results of the proposed and conventional LPTNs is presented. The need for the proposed LPTN was then emphasized by explaining the relationship between the motor size and the coil temperature.

Among the design factors of the motor, the temperature of the coil (hot spot) is crucial, and the proposed model enables accurate temperature prediction during fault operation; this is useful when designing a motor for use in fault-tolerant systems. In addition, if the proposed LPTN is reflected in the OHP control logic, a more accurate temperature prediction is achieved than that for the conventional LPTN under fault conditions. Therefore, the limited system performance due to the motor coil temperature can be maximized. To improve the accuracy of the proposed model in the future, the contact resistance between the stator core segments and the variation in the heat-transfer coefficient must be studied based on various conditions.

References

[1] W. Zhao, L. Xu, and G. Liu, "Overview of permanent-magnet fault-tolerant machines: Topology and design," *CES Trans. Electr. Mach. Syst.*, vol. 2, no. 1, pp. 51–64, Mar. 2018.

[2] A. M. El-Refaie, "Fault-tolerant permanent magnet machines: A review," *IET Electr. Power Appl.*, vol. 5, no. 1, p. 59, 2011.

[3] Y. Zhao, H. Wang, D. Li, and R. Qian, "Fault-tolerant performance of a three-phase dual armature-winding doubly salient brushless DC generator," *IEEE Access*, vol. 6, pp. 18022–18031, 2018.

[4] Z. Mao, G. Tao, B. Jiang, and X.-G. Yan, "Adaptive compensation of traction system actuator failures for high-speed trains," *IEEE Trans. Intell. Transp. Syst.*, vol. 18, no. 11, pp. 2950–2963, Nov. 2017.

[5] Z. Mao, X.-G. Yan, B. Jiang, and M. Chen, "Adaptive fault-tolerant sliding-mode control for high-speed trains with actuator faults and uncertainties," *IEEE Trans. Intell. Transp. Syst.*, vol. 21, no. 6, pp. 2449–2460, Jun. 2020.

[6] M. Moradi and A. Fekih, "Adaptive PID-sliding-mode fault-tolerant control approach for vehicle suspension systems subject to actuator faults," *IEEE Trans. Veh. Technol.*, vol. 63, no. 3, pp. 1041–1054, Mar. 2014.

[7] Y. Wang, Y. Song, H. Gao, and F. L. Lewis, "Distributed fault-tolerant control of virtually and physically interconnected systems with application to high-speed trains under traction/braking failures," *IEEE Trans. Intell. Transp. Syst.*, vol. 17, no. 2, pp. 535–545, Feb. 2016.

[8] H. Yang, V. Cocquempot, and B. Jiang, "Optimal fault-tolerant path-tracking control for 4WS4WD electric vehicles," *IEEE Trans. Intell. Transp. Syst.*, vol. 11, no. 1, pp. 237–243, Mar. 2010.

[9] L. Zhang, Y. Fan, R. Cui, R. D. Lorenz, and M. Cheng, "Fault-tolerant direct torque control of five-phase FTFSCW-IPM motor based on analogous three-phase SVPWM for electric vehicle applications," *IEEE Trans. Veh. Technol.*, vol. 67, no. 2, pp. 910–919, Feb. 2018.

[10] L. Pugi, T. Favilli, L. Berzi, E. Locorotondo, and M. Pierini, "Brake blending and torque vectoring of road electric vehicles: A flexible approach based on smart torque allocation," *Int. J. Electro. Hybrid Vehicles*, vol. 12, no. 2, pp. 87–115, 2020.

[11] Y. Yang, Q. Tang, L. Bolin, and C. Fu, "Dynamic coordinated control for regenerative braking system and anti-lock braking system for electrified vehicles under emergency braking conditions," *IEEE Access*, vol. 8, pp. 172664–172677, 2020.

[12] J.-Y. Hwang, H. Lee, J.-H. Kim, J.-H. Kim, and B.-H. Kwak, "Coordinated control of the brake control system and the driveline control system," in *Proc. IEEE Int. Conf. Control, Autom. Syst.*, Dec. 2007, pp. 356–361.

[13] L. Pugi, F. Grasso, M. Pratesi, M. Cipiani, and A. Bartolomei, "Design and preliminary performance evaluation of a four wheeled vehicle with degraded adhesion conditions," *Int. J. Electro. Hybrid Vehicles*, vol. 9, no. 1, pp. 1–32, 2017.

[14] W. Li, H. Du, and W. Li, "Four-wheel electric braking system configuration with new braking torque distribution strategy for improving energy recovery efficiency," *IEEE Trans. Intell. Transp. Syst.*, vol. 21, no. 1, pp. 87–103, Jan. 2020.

[15] N. Ertugrul and P. P. Acarnley, "Indirect rotor position sensing in real time for brushless permanent magnet motor drives," *IEEE Trans. Power Electron.*, vol. 13, no. 4, pp. 608–616, Jul. 1998.

[16] N. Matsui, "Sensorless PM brushless DC motor drives," *IEEE Trans. Ind. Electron.*, vol. 43, no. 2, pp. 300–308, Apr. 1996.

[17] S. Ostlund and M. Brokemper, "Sensorless rotor-position detection from zero to rated speed for an integrated PM synchronous motor drive," *IEEE Trans. Ind. Appl.*, vol. 32, no. 5, pp. 1158–1165, Sep. 1996.

[18] T. Aihara, A. Toba, T. Yanase, A. Mashimo, and K. Endo, "Sensorless torque control of salient-pole synchronous motor at zero-speed operation," *IEEE Trans. Power Electron.*, vol. 14, no. 1, pp. 202–208, Jan. 1999.

[19] P. L. Jansen and R. D. Lorenz, "Transducerless position and velocity estimation in induction and salient AC machines," *IEEE Trans. Ind. Appl.*, vol. 31, no. 2, pp. 240–247, Mar. 1995.

[20] F. Cupertino, A. Guagnano, A. Altomare, and G. Pellegrino, "Position estimation delays in signal injection-based sensorless PMSM drives," in *Proc. 3rd IEEE Int. Symp. Sensorless Control for Electr. Drives (SLED)*, Sep. 2012, pp. 1–6.

[21] J.-H. Jang, S.-K. Sul, J.-I. Ha, K. Ide, and M. Sawamura, "Sensorless drive of SMPM motor by high frequency signal injection," in *Proc. 17th Annu. IEEE Appl. Power Electron. Conf. Expo. (APEC)*, Mar. 2002, pp. 279–285.

[22] H. Kim, J. Son, and J. Lee, "A high-speed sliding-mode observer for the sensorless speed control of a PMSM," *IEEE Trans. Ind. Electron.*, vol. 58, no. 9, pp. 4069–4077, Sep. 2011.

[23] M. X. Bui, M. F. Rahman, and D. Xiao, "Sensorless control of interior permanent magnet synchronous machines based on the combination of the modified FPE method and SMO," in *Proc. IEEE 9th Int. Symp. Sensorless Control Elect. Drives (SLED)*, Sep. 2018, pp. 126–131.

[24] B. Allotta, P. D'Adamio, L. Nocentini, L. Paolucci, and L. Pugi, "Next generation of smart sensorless drives for sustainable underwater vehicles," in *Proc. IEEE 16th Int. Conf. Environ. Electr. Eng. (EEEIC)*, Jun. 2016, vol. 49, no. 21, pp. 481–486.

[25] P. H. Mellor, D. Roberts, and D. R. Turner, "Lumped parameter thermal model for electrical machines of TEFC design," *IEE Proc. B, Electr. Power Appl.*, vol. 138, no. 5, pp. 205–218, Sep. 1991.

[26] B.-H. Lee, K.-S. Kim, J.-W. Jung, J.-P. Hong, and Y.-K. Kim, "Temperature estimation of IPMSM using thermal equivalent circuit," *IEEE Trans. Magn.*, vol. 48, no. 11, pp. 2949–2952, Nov. 2012.

Authorized licensed use limited to: Hanyang University. Downloaded on June 22,2022 at 01:52:54 UTC from IEEE Xplore. Restrictions apply.

[27] A. Boglietti, A. Cavagnino, and D. A. Staton, "TEFC induction motors thermal models: A parameter sensitivity analysis," *IEEE Trans. Ind. Appl.*, vol. 41, no. 3, pp. 756–763, May 2005.
[28] A. Boglietti, A. Cavagnino, and D. Staton, "Determination of critical parameters in electrical machine thermal models," *IEEE Trans. Ind. Appl.*, vol. 44, no. 4, pp. 1150–1159, Jul. 2008.
[29] D. A. Staton and A. Cavagnino, "Convection heat transfer and flow calculations suitable for electric machines thermal models," *IEEE Trans. Ind. Electron.*, vol. 55, no. 10, pp. 3509–3516, Oct. 2008.
[30] D. A. Staton, A. Boglietti, and A. Cavagnino, "Solving the more difficult aspects of electric motor thermal analysis in small and medium size industrial induction motors," *IEEE Trans. Energy Convers.*, vol. 20, no. 3, pp. 620–628, Sep. 2005.
[31] A. Boglietti, A. Cavagnino, M. Parvis, and A. Vallan, "Evaluation of radiation thermal resistances in industrial motors," *IEEE Trans. Ind. Appl.*, vol. 42, no. 3, pp. 688–693, May 2006.
[32] S. Ayat, H. Liu, M. Kulan, and R. Wrobel, "Estimation of equivalent thermal conductivity for electrical windings with high conductor fill factor," in *Proc. IEEE Energy Convers. Congr. Expo. (ECCE)*, Sep. 2018, pp. 6529–6536.
[33] N. Simpson, R. Wrobel, and P. H. Mellor, "Estimation of equivalent thermal parameters of impregnated electrical windings," *IEEE Trans. Ind. Appl.*, vol. 49, no. 6, pp. 2505–2515, Nov. 2013.
[34] Y. A. Cengel and A. J. Ghajar, *Heat and Mass Transfer, Fundamentals and Applications*, 5th ed. New York, NY, USA: McGraw-Hill, 2015.
[35] D. A. Howey, P. R. N. Childs, and A. S. Holmes, "Air-gap convection in rotating electrical machines," *IEEE Trans. Ind. Electron.*, vol. 59, no. 3, pp. 1367–1375, Mar. 2012.
[36] J. Nerg, M. Rilla, and J. Pyrhonen, "Thermal analysis of radial-flux electrical machines with a high power density," *IEEE Trans. Ind. Electron.*, vol. 55, no. 10, pp. 3543–3554, Oct. 2008.
[37] A. B. Nachouane, A. Abdelli, G. Friedrich, and S. Vivier, "Numerical study of convective heat transfer in the end regions of a totally enclosed permanent magnet synchronous machine," *IEEE Trans. Ind. Appl.*, vol. 53, no. 4, pp. 3538–3547, Jul. 2017.
[38] A. Boglietti, A. Cavagnino, D. A. Staton, M. Popescu, C. Cossar, and M. I. McGilp, "End space heat transfer coefficient determination for different induction motor enclosure types," *IEEE Trans. Ind. Appl.*, vol. 45, no. 3, pp. 929–937, May/Jun. 2009.
[39] A. Boglietti, E. Carpaneto, M. Cossale, and S. Vaschetto, "Stator-winding thermal models for short-time thermal transients: Definition and validation," *IEEE Trans. Ind. Electron.*, vol. 63, no. 5, pp. 2713–2721, May 2016.
[40] N. Simpson, T. Duggan, P. H. Mellor, and J. D. Booker, "Measurement of the thermal characteristics of a stator-housing interface," in *Proc. IEEE 11th Int. Symp. Diag. Electr. Mach., Power Electron. Drives (SDEMPED)*, Aug. 2017, pp. 557–564.
[41] R. Camilleri, M. D. McCulloch, and D. A. Howey, "Experimental investigation of the thermal contact resistance in shrink fit assemblies with relevance to electrical machines," in *Proc. 7th IET Int. Conf. Power Electron., Mach. Drives (PEMD)*, Manchester, U.K., 2014, pp. 1–9.
[42] V. Ghorbanian, S. Hussain, S. Hamidizadeh, R. Chromik, and D. Lowther, "The role of temperature-dependent material properties in optimizing the design of permanent magnet motors," *IEEE Trans. Magn.*, vol. 54, no. 3, Mar. 2018, Art. no. 8101104.
[43] T. Sebastian, "Temperature effects on torque production and efficiency of PM motors using NdFeB magnets," *IEEE Trans. Ind. Appl.*, vol. 31, no. 2, pp. 353–357, Mar./Apr. 1995.
[44] R. Yabiku, R. Fialho, L. Teran, M. E. Ramos, and N. Kawasaki, "Use of thermal network on determining the temperature distribution inside electric motors in steady-state and dynamic conditions," *IEEE Trans. Ind. Appl.*, vol. 46, no. 5, pp. 1787–1795, Sep. 2010.
[45] M. Martinovic *et al.*, "Influence of winding design on thermal dynamics of permanent magnet traction motor," in *Proc. Int. Symp. Power Electron., Electr. Drives, Autom. Motion*, Jun. 2014, pp. 397–402.
[46] D. C. Montgomery, L. Custer, and D. R. McCarville, *Design and Analysis of Experiments*. New York, NY, USA: Wiley; 2009.
[47] T. M. Cioppa and T. W. Lucas, "Efficient nearly orthogonal and space-filling latin hypercubes," *Technometrics*, vol. 49, no. 1, pp. 45–55, Feb. 2007.
[48] L. Pronzato and W. G. Müller, "Design of computer experiments: Space filling and beyond," *Statist. Comput.*, vol. 22, no. 3, pp. 681–701, May 2012.
[49] F. Qi, M. Schenk, and R. W. De Doncker, "Discussing details of lumped parameter thermal modeling in electrical machines," in *Proc. 7th IET Int. Conf. Power Electron., Mach. Drives (PEMD)*, 2014, pp. 2.11.04–2.11.04.
[50] D. Staton, S. J. Pickering, and D. Lampard, "Recent advancement in the thermal design of electric motors," in *Proc. Fall Tech. Conf. (SMMA)*, Oct. 2001, pp. 1–11.

Baik-Kee Song received the B.S. degree in mechanical engineering and the M.S. degree in automotive engineering from Hanyang University, Seoul, South Korea, in 2009 and 2011, respectively, where he is currently pursuing the Ph.D. degree in automotive engineering.

His research interests include electro-magnetic design of motor and motor thermal analysis using equivalent circuit.

Jun-Woo Chin received the bachelor's degree in mechanical engineering from Hanyang University, Seoul, South Korea, in 2014, where he is currently pursuing the Ph.D. degree in automotive engineering. His research interests are the design, losses, and multi-physics analysis of electric machines for mechatronics systems, such as automotive applications.

Dong-Min Kim received the B.S. degree in electronic system engineering and the Ph.D. degree in automotive engineering from Hanyang University, Seoul, South Korea, in 2013 and 2021, respectively.

In 2021, he was a Postdoctoral Researcher with Hanyang University. Since 2021, he has been with Honam University, Gwangju, South Korea, where he is currently an Assistant Professor. His research interests include design optimization of electric machines for automotive and industrial applications, modeling and optimization of electric vehicles, hybrid electric vehicles, and fuel cell electric vehicles.

Kyu-Yun Hwang received the B.S. degree in electronic and computer engineering, and the Ph.D. degree in electronics, electrical, control, and instrumentation engineering from Hanyang University, Ansan, South Korea, in 2005 and 2021, respectively. From 2010 to 2012, he was a Research Engineer with Komotek Company Ltd., Seongnam, South Korea. Since 2012, he has been a Research Engineer with Mando, Seongnam. His research interest includes design, analysis, and optimization of electric machines.

Myung-Seop Lim (Member, IEEE) received the bachelor's degree in mechanical engineering and the master's and Ph.D. degrees in automotive engineering from Hanyang University, Seoul, South Korea, in 2012, 2014 and 2017, respectively.

From 2017 to 2018, he was a Research Engineer with Hyundai Mobis, Yongin, South Korea. From 2018 to 2019, he was an Assistance Professor with Yeungnam University, Daegu, South Korea. Since 2019, he has been with Hanyang University, where he is currently an Assistant Professor. His research interests include electromagnetic field analysis and multi-physics analysis of electric machinery for mechatronics systems, such as automotive and robot applications.

Authorized licensed use limited to: Hanyang University. Downloaded on June 22,2022 at 01:52:54 UTC from IEEE Xplore. Restrictions apply.